



A dipole pattern of orbital-scale precipitation oxygen isotope variation in North African monsoon region and the driving mechanism

Chengwei Ji^{1,2}, Qin Wen^{1,2*}, Zhengyu Liu³, Jian Liu^{1,2,4}, Deliang Chen⁵, Liang Ning^{1,2}, Mi Yan^{1,2}, and Qiuzhen Yin⁶

¹State Key Laboratory of Climate System Prediction and Risk Management / Key Laboratory for Virtual Geographic Environment of Ministry of Education / Jiangsu Center for Collaborative Innovation in Geographical Information Resource Development and Application, Nanjing, 210023, China

- ²School of Geography, Nanjing Normal University, Nanjing, 210023, China
 - ³Department of Geography, Ohio State University, Columbus, OH 43210, USA
 - ⁴Jiangsu Provincial Key Laboratory for Numerical Simulation of Large-Scale Complex Systems, School of Mathematical Science, Nanjing Normal University, Nanjing, 210023, China
 - ⁵Department of Earth System Science, Tsinghua University, Beijing, 100084, China
- 6Earth and Climate Research Center, Earth and Life Institute, Université catholique de Louvain, 1348, Louvain-la-Neuve, Belgium

Correspondence to: Qin Wen(qin.wen@njnu.edu.cn)

Abstract. Variations in North African (NAF) monsoon have pronounced socioeconomic impacts on many Western African countries. The orbital-scale NAF monsoon variation is reconstructed using speleothem δ¹⁸O (δ¹⁸O_c) records from caves. However, the climate meaning of these records is not well-known. δ¹⁸O_c in tropical monsoon regions is primarily determined by precipitation δ¹⁸O (δ¹⁸O_p). Here, we use the isotope-enabled Community Earth System Model (iCESM) to investigate the climate interpretation of δ¹⁸O_c in the NAF monsoon region on the orbital timescale. Our analysis shows that both δ¹⁸O_p and NAF monsoon rainfall exhibit a distinct precession signal. Enhanced Northern Hemisphere summer insolation (NHSI) intensifies land-sea thermal contrast, leading to strengthened monsoon circulation and increased NAF monsoon rainfall. However, the δ¹⁸O_p presents a spatially dipole pattern, with depletion in the southern NAF and enrichment in the north. Tagging experiments further reveal that, while depletion in the south is driven by increased rainfall in upstream regions, enrichment in the north results from shifts in moisture sources, with a reduced contribution from distant sources and an increased influence of local sources. This work provides new insights into understanding the climatic meaning of isotopic records in NAF region and underscores the complex spatial features of isotopic signals compared to rainfall responses.





1 Introduction

35

45

The North African (NAF) monsoon region is one of the most vulnerable hotspots under climate change (Lézine et al., 2011). Monsoon variability in this region exerts substantial environmental and socioeconomic effects, particularly across Sahelian countries where economies rely heavily on rainfed agriculture (Sultan et al., 2005; Sultan and Gaetani, 2016). At the orbital timescale, the NAF region is highly sensitive to orbital forcing and has experienced dramatic fluctuations between wet and dry periods (deMenocal, 2004; deMenocal and Tierney, 2012; Ehrmann et al., 2017; Kutzbach et al., 2020). These changes not only drive the early human migration to the Nile Basin and the rise of agricultural civilization (McDougall et al., 2005; Vaks et al., 2007; Kutzbach et al., 2020), but also have profound impacts on Asian monsoon, ENSO activity, and even the polar ice sheets through atmospheric teleconnections (Muschitiello et al., 2015; Pausata et al., 2020). Given the important role of NAF monsoon in the global climate change, a clear understanding of its past evolution is critical for improving predictions of its future behavior.

The cave speleothem oxygen isotope ($\delta^{18}O_c$) records have been widely used for reconstructing past hydrological variations in monsoon regions (Wang et al., 2001; Bar-Matthews et al., 2003; Cruz et al., 2005; Cheng et al., 2013). Under conditions of isotopic equilibrium, the $\delta^{18}O_c$ depends on the cave temperature and the precipitation $\delta^{18}O$ ($\delta^{18}O_p$). In the NAF region, the δ¹⁸O_c shows a strong precessional signal, with the enhanced Northern Hemisphere summer insolation (NHSI) corresponding to a depleted δ^{18} O value (Bar-Matthews et al., 2003; Brahim et al., 2023). Meanwhile, other moisture-related proxies from lakes (Kohfeld and Harrison, 2000; Armitage et al., 2015), terrigenous sediment (deMenocal et al., 2000; Revel et al., 2010; Ehrmann et al., 2016; Skonieczny et al., 2019; Blanchet et al., 2021), and pollen (Lézine et al., 2005; Fersi et al., 2016) show that a higher NHSI corresponds to stronger NAF rainfall. Therefore, the observed cave $\delta^{18}O_c$ and moisture proxies exhibit a significant "amount effect" (Dansgaard, 1964; Rozanski et al., 1993) in the NAF region, with more negative δ¹⁸O_c value corresponding to more humid conditions. However, it is still unclear whether the NAF δ^{18} O_c signal responds primarily to changes in local rainfall or is controlled by other factors. This question arises because a growing number of studies have shown that many factors other than local rainfall amount can affect $\delta^{18}O_p$, including changes in the relative contribution of moisture sources (Cole et al., 1999; Vuille et al., 2003), isotope composition during convective activity (Lee and Fung, 2007; Risi et al., 2008; Kurita, 2013; Moore et al., 2014) and upstream rainfall effects (Lee et al., 2009; Pausata et al., 2011; Liu et al., 2014; Shi et al., 2025). These factors may contribute to isotope variations, thereby complicating the interpretation of isotope data in paleoclimate.

Numerous modeling studies have been conducted in the past to investigate the NAF monsoon. For example, Kutzbach and Liu (1997) conducted middle Holocene simulations with a general circulation model that asynchronously couples the atmosphere and the ocean. Their simulations show that increased insolation induces an intensified land-sea thermal contrast and enhanced summer monsoon rainfall. Similarly, Tuenter et al. (2003) used an Earth system model of intermediate complexity (ECBilt) to analyze orbital-scale signals over Africa. They demonstrate that a stronger and more northward



65



monsoon over NAF occurs at times of minimum precession or maximum obliquity, when boreal summer insolation is high. This rainfall enhancement is attributed to a stronger land-sea thermal contrast, intensified low-level monsoonal circulation, and increased moisture transport. Similar results are also found in Bosmans et al. (2015) using the EC-Earth model. To further explore the evolution of the NAF monsoon, Kutzbach et al. (2020) performed transient simulations covering the past 140,000 years using a dynamic atmosphere-ocean general circulation model with higher resolution. Their simulations show that orbital precession causes high seasonality in Northern Hemisphere (NH) insolation, with stronger and northward extended summer monsoon rainfall and increased winter rains in the Mediterranean Basin. These combined effects increase vegetation and narrow the width of the Saharan-Arabian desert. Despite these advances, most existing model studies have focused primarily on monsoon rainfall due to the absence of water isotope modules in these climate models.

Over the past few decades, isotope-enabled models have evolved as valuable and well-established tools for improving our understanding of the relationship between water isotopes and climate variables. Herold and Lohmann (2009) examined the effect of orbital forcing on the NAF $\delta^{18}O_p$ using an isotope-enabled General Circulation Model (ECHAM4). They identify a dipole pattern in $\delta^{18}O_p$ response to orbital-induced insolation increase, characterized by enrichment in the western NAF and depletion in the eastern region. The western enrichment is interpreted as a result of reduced upstream rainfall depletion due to decreased rainfall over the Atlantic, while the eastern depletion is attributed to increased local rainfall and enhanced moisture advection from the Atlantic. A similar $\delta^{18}O_p$ dipole pattern was reported by Battisti et al. (2014), who suggested that $\delta^{18}O_p$ over northeast Africa is primarily controlled by changes in summer isotopic composition. However, other modeling studies have demonstrated a clear "amount effect" in the temporal $\delta^{18}O_p$ -rainfall relationship across the NAF monsoon region, with significant $\delta^{18}O_p$ depletion coinciding with increased monsoon rainfall (Cauquoin et al., 2019; Shi et al., 2023). This coherent depletion pattern appears inconsistent with the previously identified dipole structure. More recently, Shi et al. (2025) examined spatial and temporal variations in both rainfall and $\delta^{18}O_p$ across the NAF region based on 24 timeslice experiments covering a full precession cycle. Their results show widespread $\delta^{18}O_p$ depletion throughout the NAF, but also reveal a positive temporal $\delta^{18}O_p$ -rainfall relationship in some inland areas, contradicting the classical "amount effect". For these regions, the authors propose that δ¹⁸O_p variations are influenced mainly by rainfall changes in upstream areas rather than local rainfall, consistent with earlier proposed upstream depletion processes (Pausata et al., 2011; Liu et al., 2014; Tabor et al., 2018). Therefore, despite extensive modeling efforts focused on NAF $\delta^{18}O_p$, the interpretations of $\delta^{18}O_p$ vary among different models. The understanding of the relationship between $\delta^{18}O_p$ and NAF monsoon climate is still underway.

In this study, we use the isotope-enabled fully coupled Community Earth System Model (iCESM) to examine the response of $\delta^{18}O_p$ to orbital forcing over the NAF region. Our results indicate that both $\delta^{18}O_p$ and NAF monsoon rainfall exhibit a distinct precession signal. During periods of high NHSI, rainfall increases uniformly across the NAF region, whereas $\delta^{18}O_p$ exhibits a dipole pattern, characterized by depletion in the southern NAF and enrichment in the northern NAF. Moisture tagging experiments further reveal that the depletion in the south is primarily caused by enhanced upstream rainfall, while





the enrichment in the north arises from shifts in moisture sources associated with atmosphere circulation. The paper is arranged as follows. Section 2 describes the Data and methods; Section 3 presents the Data-model comparison; Sections 4 and 5 discuss the mechanisms underlying rainfall and $\delta^{18}O_p$ changes, respectively; and Section 6 provides the Conclusions.

2 Data and methods

100

105

110

120

125

2.1 The 150,000-year simulation

In this study, the isotope-enabled Community Earth System Model (iCESM) is employed, which comprises atmosphere model (CAM5), land model (CLM4), sea ice model (CICE4), and ocean model (POP2) (Brady et al., 2019). The CAM5 has a horizontal resolution of $1.9^{\circ} \times 2.5^{\circ}$ (latitude × longitude) and 30 hybrid vertical levels (Neale et al., 2010). By parameterizing physical processes (such as evaporation, condensation, advection) and isotope fractionation equations (such as Rayleigh fractionation, kinetic effect), the model can dynamically track the oxygen isotope transport and fractionation effect during the water cycle, thus realizing the isotopic tracing of the complete path from evaporation in the ocean source region to rainfall on land (Nusbaumer et al., 2017). The CLM4 shares the same horizontal grid as the atmosphere model (Oleson et al., 2010). The POP2 and CICE4 share a nominal horizontal resolution of 1° , with POP2 configured with 60 vertical layers (Smith et al., 2010; Hunke, 2010). The iCESM has been successfully applied in multi-scale climate studies to investigate mechanisms linking the hydrological cycle and isotopic signals (Tabor et al., 2018; Hu et al., 2019; He et al., 2021; Bao et al., 2023; Wen et al., 2024). It has been shown to adequately capture key features of the monsoon system (Wen et al., 2024) as well as the spatial and temporal patterns of $\delta^{18}O_p$, albeit with smaller values (Brady et al., 2019; Nusbaumer et al., 2017).

We conduct a 150,000-year transient simulation that is driven solely by variations in Earth's orbital parameters (i.e., precession, obliquity, and eccentricity) (Berger, 1978). All other boundary conditions, such as greenhouse gas concentrations, ice sheet extent, and vegetation distribution, are held constant at pre-industrial levels (Wen et al., 2024). The orbital-only forcing simulation is justified for NAF analysis, as the precessional signal dominates the climate variability in this region (Pokras and Mix, 1987; Patricola and Cook, 2007; Weber and Tuenter, 2011; Cheng et al., 2020).

The experiment starts 170,000 years ago with the last 150,000 years used for analysis. Due to the limitation of computational resources, the experiment is accelerated by 100-time to improve efficiency. That is, at the end of each year's simulation, we advance the orbital parameters by 100 years, so the actual length of our simulation is 1500 years. This acceleration scheme is suitable for the monsoon analysis given that the response time of the atmosphere-upper ocean system is much faster than the shortest orbital cycle (Kutzbach et al., 2008; Wen et al., 2024). The previous analysis shows that the acceleration method leads to a delayed response only in the deep-ocean temperature, but has little impact on the near-surface quantities like temperature and precipitation (Lorenz and Lohmann, 2004; Timm and Timmermann, 2007; Yin and Berger, 2015). Since



130

135



this study focuses on surface ocean-atmospheric conditions, the 100-factor acceleration scheme would not affect the conclusions regarding the NAF monsoon region.

It is noted that the simulation in this study is driven only by orbital forcing and lacks other external forcing. Although other factors (e.g., ice cover, greenhouse gases, sea-land distribution, and topography) also influence the variability of the monsoon climate system, they do not fundamentally change the perception that solar radiation is the main driving factor (Cheng et al., 2020). Roe et al. (2016) conducted a set of idealized experiments to compare the impact of each of five separate factors (orbital configuration, atmospheric carbon dioxide, glacial lower boundary conditions, displacement of the Indian subcontinent, an inland sea) on climate. Their results show that among all factors, the orbital insolation variation has the largest impact, while the other factors have only small effect on the African monsoon rainfall and $\delta^{18}O_p$. Therefore, our simulation considering only orbital forcing is reasonable, but due to lacking land surface feedback processes such as dust and vegetation, our simulation could underestimate the northward extension of the monsoon (Waldmann et al., 2010; Pausata et al., 2016; Tierney et al., 2017; Messori et al., 2019).

2.2 Precipitation $\delta^{18}O$ ($\delta^{18}O_p$) and calcite $\delta^{18}O$ ($\delta^{18}O_c$) in iCESM

Since the water isotope records cannot resolve the seasonal signal, we analyze the annual precipitation-weighted $\delta^{18}O$ ($\delta^{18}O_p$) as in the following equations:

$$\delta^{18}O_p = \sum_{m=1}^{12} \delta^{18}O_m \cdot \frac{P_m}{p},\tag{1}$$

where m denotes the calendar month, P_m is precipitation from month m, $\delta^{18}O_m$ is the $\delta^{18}O$ in precipitation from month m, and P is annual total precipitation.

 δ^{18} O_c can be calculated following O'Neil et al (1969):

145
$$\delta^{18}O_c = \delta^{18}O_{w-PDB} + 2.70 \times 10^6/T^2 - 3.29$$
, (2)

where T represents the cave temperature, which is approximated by the annual mean surface air temperature in the model. $\delta^{18}O_{w-PDB}$ can be converted from $\delta^{18}O_{p}$ according to Coplen et al. (1983):

$$\delta^{18}O_{w-PDB} = 0.97002 \times \delta^{18}O_{p-SMOW} - 29.98.$$
 (3)

2.3 Tagging experiments

In order to quantitatively analyze the different moisture sources of δ¹⁸O_p in the target region, two water tagging experiments are carried out at the times of 127 ka (high NHSI periods) and 116 ka (low NHSI periods) using the atmospheric model iCAM5.3. These two time slices correspond to the period of greatest changes in solar insolation across the past 150,000 years, and the climate response between these two periods can infer the climate evolution at the orbital timescale. The external forcing in both tagging experiments is based on the orbital parameters specific to their respective periods. The





- boundary conditions are derived from a 1000-year climatological mean state centered around each corresponding period, as obtained from the iCESM experiment. The experiments can track water vapor evaporating from the source regions until they follow the hydrological processes in the model to the region where they rain out (sink region). The global source regions have been divided into 25 subregions, with 13 covering the ocean and the rest covering the land (Wen et al., 2024). Each tagging experiment is integrated for 40 years, with the last 20 years used for analysis.
- Here, to study the NAF, the original 25 source regions are grouped into five regions according to their relative importance for NAF hydroclimate variability: the North Atlantic Ocean, the South Atlantic Ocean, the Indian Ocean, the African continent, and the rest of the globe. Thus, the rainfall and $\delta^{18}O_p$ at a grid point are the sums from all five source regions:

$$P = \sum_{i=1}^{5} P_i , \ \delta^{18} O_p = \sum_{i=1}^{5} \delta^{18} O_i \cdot \frac{P_i}{p}, \tag{4}$$

where P_i and $\delta^{18}O_i$ represent the rainfall and $\delta^{18}O_p$ from the i-th tagging source region, respectively.

165 **2.4 Decomposition of \delta^{18}O**_p

The $\delta^{18}O_p$ response between high and low NHSI periods, referred to as $\Delta\delta^{18}O_p$, can be decomposed into two parts: the change associated with the precipitation weight $\Delta\left(\frac{P_i}{P}\right)$ and the change in the value of isotope ratio $\Delta\delta^{18}O_{pi}$:

$$\Delta \delta^{18} O_p = \sum_{i=1}^5 \delta^{18} O_{pi} \cdot \Delta \left(\frac{P_i}{P} \right) + \sum_{i=1}^5 \frac{P_i}{P} \cdot \Delta \delta^{18} O_{pi} . \tag{5}$$

The first part is shown in Fig. 7, which is associated with climatology isotope ratio $\delta^{18}O_{pi}$ and the change in precipitation weight. The second part is shown in Fig. 8, which can be further decomposed into three terms. The first term denotes the vapor $\delta^{18}O_i$ in the source region, which is produced by the net effect of local rainfall and evaporation at the source region. The second term denotes the en route depletion of vapor $\delta^{18}O_i$ due to rainout along its trajectory from the source region to the sink region. The third term denotes the local condensation enrichment due to the transition from vapor to rainfall in the sink region, along with any post-condensation processes such as rain evaporation. These terms are written as follows:

$$\Delta \delta^{18} O_{pi} \cdot \frac{P_i}{P} = \Delta \left(\delta^{18} O_{v,source} \right)_i \cdot \frac{P_i}{P}$$

$$+ \Delta \left(\delta^{18} O_{v,sink} - \delta^{18} O_{v,source} \right)_i \cdot \frac{P_i}{P} .$$

$$+ \Delta \left(\delta^{18} O_{p,sink} - \delta^{18} O_{v,sink} \right)_i \cdot \frac{P_i}{P} .$$

$$(6)$$

2.5 Moist static energy budget

175

The column-integrated moist static energy (MSE) budget is used to accurately calculate the energy changes in the atmosphere column and to better understand the mechanisms of rainfall changes in the monsoon region. The MSE balance equation is referenced from Hill et al. (2017) and Wen et al. (2022).

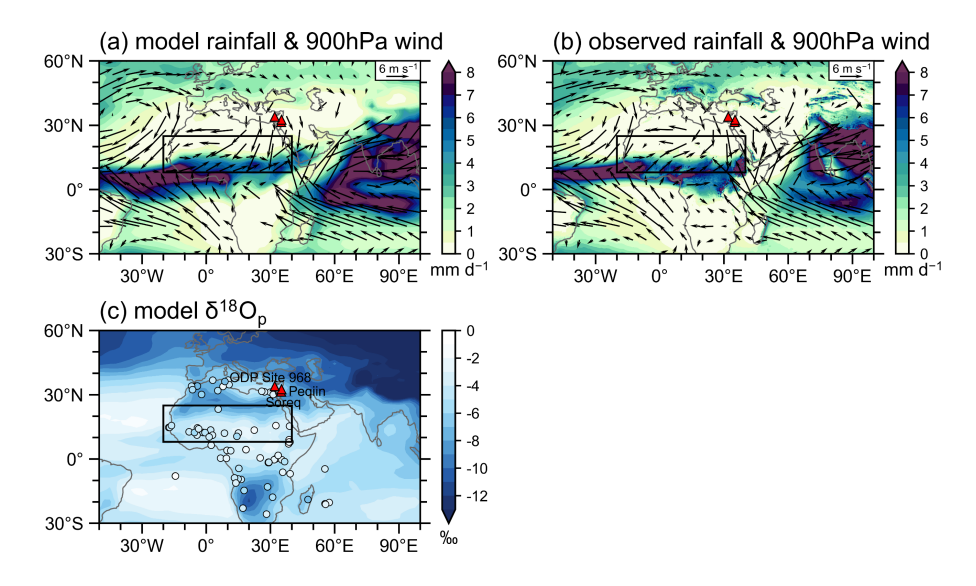




180
$$\left\{ \overline{\omega} \frac{\partial \overline{h}}{\partial v} \right\} \approx \overline{F}_{net} - \left\{ \overline{v} \cdot \nabla_{p} \overline{h} \right\} - \left\{ \nabla_{p} \cdot \overline{(v'h')} \right\} - \left\{ \partial_{t} \overline{h} \right\},$$
 (7)

where $\{\cdot\} = \int_0^{P_S} \cdot \left(\frac{dp}{g}\right)$, denotes the column integration from the surface P_S to the top of the atmosphere. h represents the MSE: $h = c_p T + gz + L_v q$. F_{net} is the net energy flux into the atmosphere column. Overbars are the monthly mean and primes are the transient eddy. Conceptually, energetic input into the atmosphere column through its upper and lower boundaries must be balanced by vertical MSE advection $(\{\overline{\omega}\partial_p\overline{h}\})$, horizontal MSE advection $(\{\overline{v}\cdot\nabla_p\overline{h}\})$, transient eddy MSE $(\{\nabla_p\cdot\overline{(v'h')}\})$, and change in total column MSE over time $(\{\partial_t\overline{h}\})$. $\{\partial_t\overline{h}\}$ can be ignored here because it is small for climatology analysis. In the vertical MSE advection term, $\{\overline{\omega}\partial_p\overline{h}\} > 0$ implies upward motion $(\overline{\omega}<0)$ since $\partial_p\overline{h}$ is almost negative in the troposphere.

3 Data-model comparison



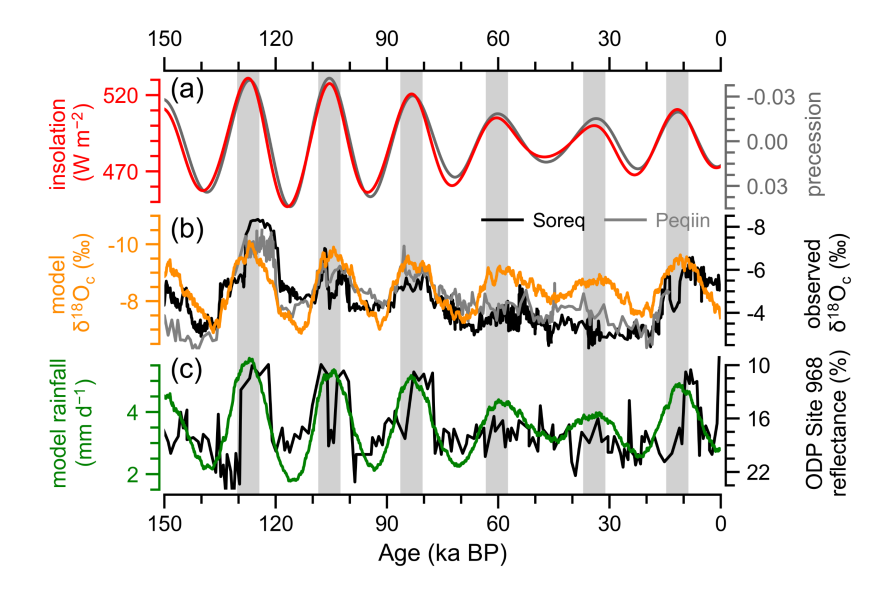
190 **Figure 1: Modern climatology of the North Africa (NAF) summer monsoon and δ¹8O_p. (a)** Simulated boreal summer (JJA) rainfall (shading; mm d⁻¹) and 900hPa wind (vector; m s⁻¹). (b) Same as (a) but for observation during 1940–2024 from ERA5 (https://cds.climate.copernicus.eu/). (c) Simulated annual precipitation-weighted δ¹8O_p (shading; ‰) and observed δ¹8O_p from GNIP (https://nucleus.iaea.org/wiser/explore/) (circle; ‰). The black rectangle region (8°N-25°N, 20°W-40°E) is the study area of the NAF monsoon and is used for subsequent regional averaging. The red triangles mark the locations of the proxy sites in Fig. 2.

195 The iCESM effectively captures the key features of modern NAF climate and δ¹⁸O_p (Fig. 1). Specifically, a low-level southwesterly flow transports humid air from the equatorial Atlantic to the African continent and converges with dry air from the Sahara, leading to heavy rainfall in the Sahel and its southern areas (Fig. 1a) (Rose et al., 2016; Selami et al., 2021; Datti et al., 2025). These features generally align with modern observations (Fig. 1b) and other model simulations (Cook and Vizy, 2019; Shi et al., 2024). The simulated NAF δ¹⁸O_p shows a north-south gradient, with more depleted values over the





Sahara and more enriched values in the tropics (shading in Fig. 1c). This pattern agrees with observations from the Global Network of Isotopes in Precipitation (GNIP) (circles in Fig. 1c) and other climate models (Cauquoin et al., 2019; Shi et al., 2023, 2025). The δ¹⁸O_p values in the Sahel and its southern regions are relatively high, likely due to their proximity to the moisture source region over the tropical Atlantic Ocean. The values gradually decrease farther inland, as the air masses undergo repeated condensation and rainfall cycles during their movement toward the continental interior (Shi et al., 2023).



205

Figure 2: Data-model comparison. (a) Northern Hemisphere summer insolation (NHSI) at 30°N (red; W m⁻²) and Precession parameter (grey) (Berger, 1978). (b) Simulated $\delta^{18}O_c$ in the NAF region (orange; ‰) and speleothem $\delta^{18}O_c$ records from Soreq Cave (black; ‰) and Peqiin Cave (grey; ‰), Israel (Bar-Matthews et al., 2003). (c) Simulated NAF rainfall (green; mm d⁻¹) and color reflectance (black; %) at 540nm from ODP Site 968, Mediterranean (Ziegler et al., 2010).

Moreover, our simulations can well reproduce the NAF monsoon evolution during the past 150,000 years (Fig. 2). In this work, the NAF monsoon region is defined as 8°N to 25°N and 20°W to 40°E, which is denoted as black box in Fig. 1. The simulated NAF δ¹8Oc (orange line in Fig. 2b) varies in phase with NHSI, exhibiting strong precessional signal. Specifically, higher NHSI corresponds to more depleted δ¹8Oc values. This is in agreement with the δ¹8Oc records from Soreq and Peqiin caves (black and grey lines in Fig. 2b), although the simulated amplitude is smaller than that in the reconstructions. It should be noted that although the Soreq and Peqiin caves are located outside the defined NAF monsoon region, their δ¹8Oc records primarily reflect hydroclimate changes influenced by the NAF monsoon. This interpretation is supported by the strong agreement between these speleothem records and marine δ¹8O data from the eastern Mediterranean Sea, where variations in seawater δ¹8O are largely controlled by freshwater input from Nile River discharge (Ayalon et al., 2002; Bar-Matthews et al., 2003; Rohling et al., 2015).





Additionally, our simulations show an increased rainfall when NHSI is high (green line in Fig. 2c), which is consistent with rainfall records from ODP Site 968 (organic-rich layers, i.e., 540 nm reflectance in Fig. 2d). The sapropel layers in this sediment core reflect deep-water anoxia and increased primary productivity, which is mainly related to the increased run-off inputs into the eastern Mediterranean driven by the NAF monsoon-induced continental rainfall (Ziegler et al., 2010; deMenocal and Tierney, 2012; Grant et al., 2016, 2017). The appearance of the sapropel layers corresponds to the intensification of the NAF monsoon rainfall. Moreover, we observe a strong negative correlation (r = -0.82) between δ¹⁸O_c and rainfall, with lower δ¹⁸O_c values accompanied by higher monsoon rainfall, suggesting that this satisfies the "amount effect" in terms of the statistical relationship. Notably, summer insolation at 30°N closely follows the orbital precession cycle, reflecting the dominance of precession on low latitude insolation (Berger and Pestiaux, 1984; Berger et al., 1993). These findings point out that the δ¹⁸O_c and rainfall variations are highly sensitive to precession-driven insolation changes, emphasizing the importance of precessional forcing in shaping low-latitude climate dynamics.

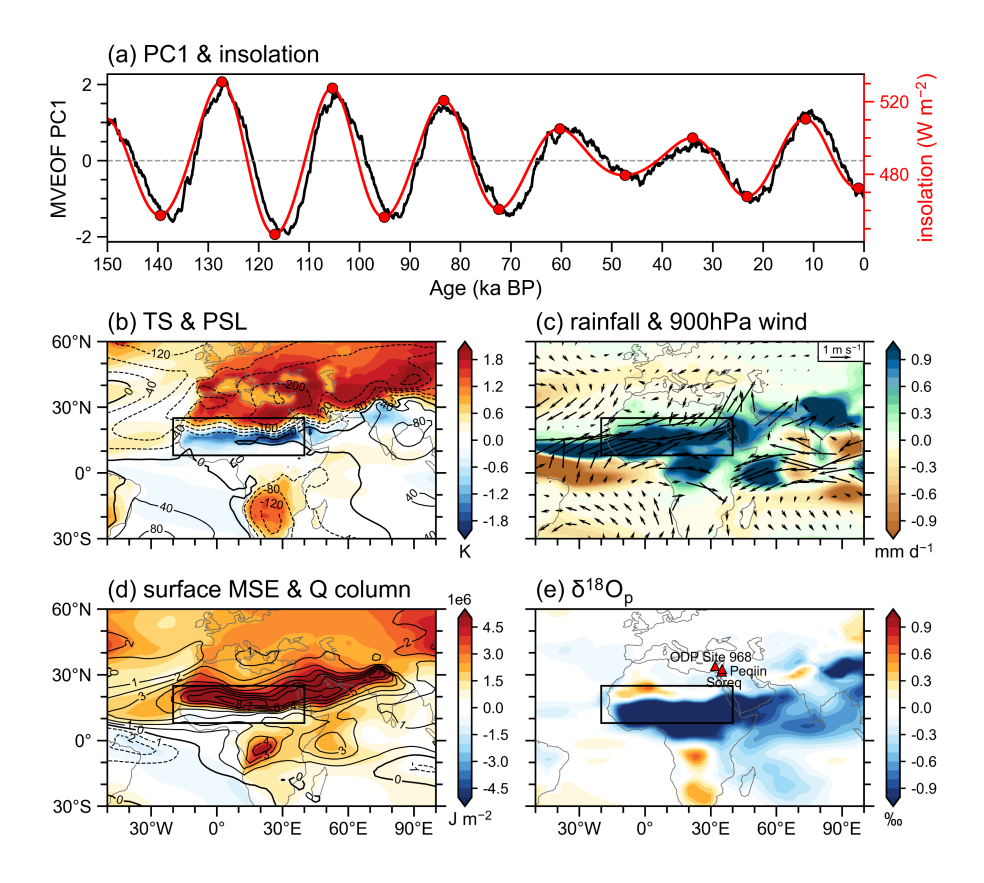


Figure 3: The general pattern of $\delta^{18}O_p$ and NAF summer climate change during the past 150,000 years. (a) Normalized principal component time series (black) of the first MVEOF mode (PC1; explained 35.6% of the total variance) between summer rainfall and $\delta^{18}O_p$ and NHSI (red; W m⁻²). The red circles represent the high and low NHSI periods used in the following composite analysis in Fig. 4. (b) surface temperature (shading; K) and sea level pressure (contour; Pa) regressed on the normalized time coefficient of PC1 [black in (a)]. (c) As in (a) but for rainfall (shading; mm d⁻¹) and 900 hPa wind (vector; m s⁻¹). (d) As in (a) but for surface moist static energy (MSE)



240



(shading; J m⁻²) and atmospheric precipitable water (contour; kg m⁻²). (e) As in (a) but for precipitation-weighted $\delta^{18}O_p$ (shading; ‰). The black rectangle is the NAF monsoon region.

We further examine the coherent response of rainfall and water isotope by conducting Multivariate Empirical Orthogonal Function (MVEOF) analysis. Previous studies have shown that the $\delta^{18}O_p$ plays a dominant role in determining the speleothem $\delta^{18}O_c$ (Cheng et al., 2012, 2016; Liu and Battisti, 2015). Therefore, for simplicity, we subsequently used $\delta^{18}O_p$ for further analyses. The results show that the explained variance of the first MVEOF mode accounts for 35% of the total variance, with the time coefficient following NHSI and exhibiting a strong precessional signal (Fig. 3a).

Spatial analysis reveals that while NHSI induces a spatially homogeneous rainfall response across the NAF region, it produces a meridional dipole pattern in $\delta^{18}O_p$ (Fig. 3c and e). Specifically, when the NHSI is high, there is a dramatic 245 warming over the Eurasian continent, which triggers the anomalous low-pressure over the continent and enhances the landsea thermal contrast (Fig. 3b). This strengthens southwesterly winds that transport moisture from the equatorial Atlantic into Africa, resulting in pronounced vapor convergence over the Sahara-Sahel region (Fig. 3c-d). Concurrently, increased surface MSE destabilizes the atmospheric column, promoting upward vertical motion (Patricola and Cook, 2007; Roe et al., 2016). Together, these processes enhance deep convection and significantly increase rainfall across the NAF monsoon region (Fig. 250 3c). Additionally, the increased cloud formation and rainfall cause a pronounced cooling between 10°N and 20°N (Patricola and Cook, 2007; Herold and Lohmann, 2009; Marzocchi et al., 2015; Wen et al., 2022). Despite this cooling, Patricola and Cook (2007) suggest that elevated low-level moisture content dominates the MSE change, further destabilizing the atmospheric column and reinforcing convection. Thus, although surface temperatures decrease in this latitudinal band (Fig. 255 3b), MSE continues to rise due to increased humidity, which is sufficient to sustain deep convection (Fig. 3d). A strengthened NAF monsoon also weakens the northeasterly winds over the Sahara, thereby reducing dust emissions. This is consistent with the dust records observed in Atlantic sediment cores located offshore at the NAF continent (Skonieczny et al., 2019; O'Mara et al., 2022; Crocker et al., 2022). Furthermore, orbitally forced Northern Hemisphere summer warming amplifies the interhemispheric temperature gradient, shifting the ITCZ northward (Schneider et al., 2014). This shift extends monsoon rainfall farther north and contracts the Saharan arid belt (Fig. 3c). 260

Since the $\delta^{18}O_c$ records evolves coherently with the NAF monsoon rainfall as in "amount effect" (Fig. 2b-c), one may expect a spatially uniformly distributed $\delta^{18}O_p$ response to insolation forcing similar to rainfall response (Fig. 3c). However, $\delta^{18}O_p$ exhibits a dipole response with increasing in the northern NAF but decreasing in the south (Fig. 3e). This implies the complex regional response of $\delta^{18}O_p$ to external forcing.

265 4 Mechanism of rainfall change

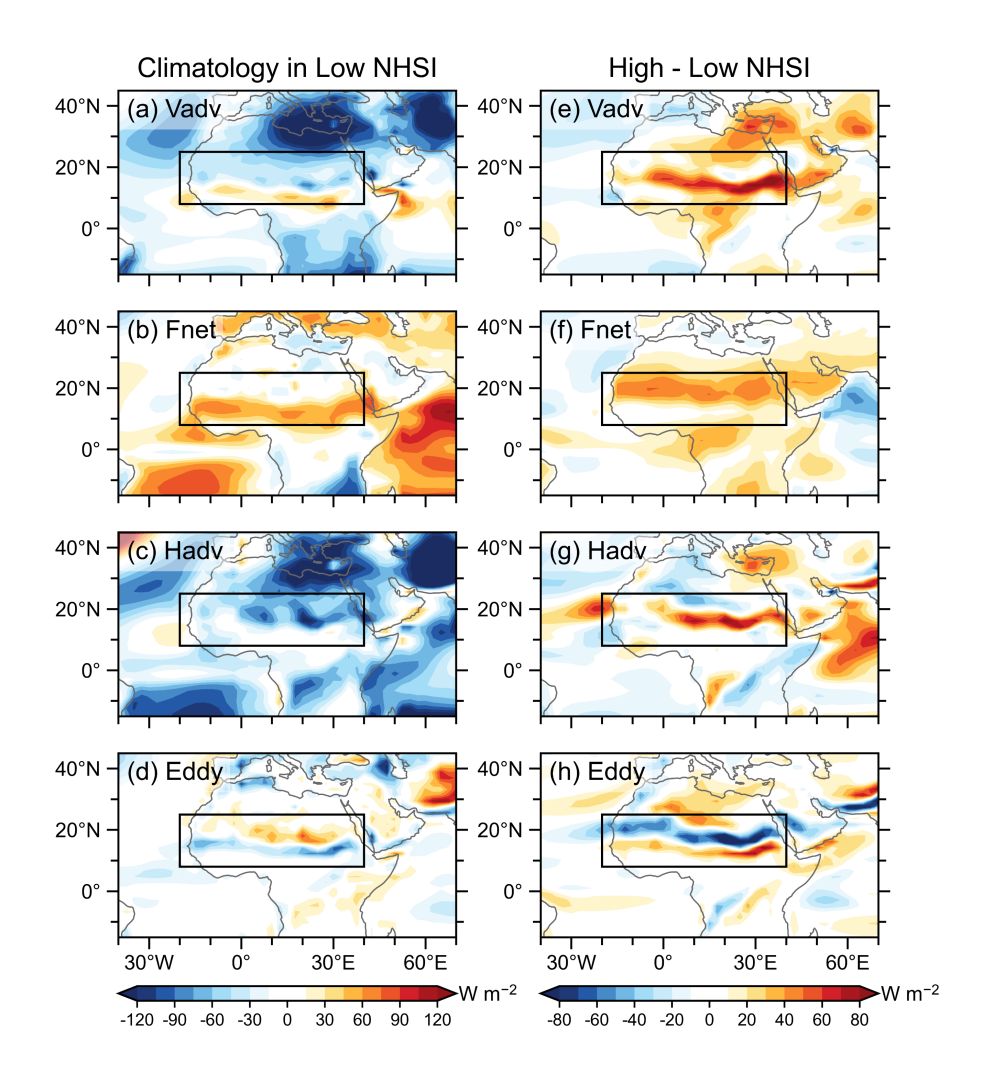
Here, we employ the MSE budget to elucidate the physical mechanisms behind monsoon rainfall responses. As previously demonstrated, the mean state exhibits intense rainfall over the Sahel and its southern regions. This rainfall is initiated by



275



strong energy input into the atmospheric column (Fig. 4b), which drives vertical MSE advection in the tropics (Fig. 4a) and, consequently, sustains deep convective rainfall in these areas (Fig. 1a). These findings align with previous studies indicating that the vertical MSE advection is primarily balanced by the net energy flux (Chen and Bordoni, 2014; Hill et al., 2017). To the north of the rainfall band, pronounced subsidence is observed (Fig. 4c), consistent with the low rainfall amounts and the presence of the Sahara Desert in this region (Fig. 1a). This suppressed convection is caused by negative horizontal enthalpy advection (Fig. 1c), in line with anticyclonic circulation and divergent sinking flow (Fig. 1a). It is noteworthy that horizontal enthalpy advection is relatively weak over tropical Africa, which appears inconsistent with the strong southwesterlies that bring abundant moisture from the equatorial Atlantic. This apparent discrepancy can be attributed to the relatively uniform spatial distribution of MSE in the region, a structure that promotes deep convection while prohibits horizontal MSE advection (Hill et al., 2017). The transient eddy term presents a meridional dipolar structure (Fig. 4d), which is opposite to the vertical advection term and likely reflects northward moisture transport by African easterly waves (Hill et al., 2017).





285

290



Figure 4: Composite analysis of summer MSE budget. (a)-(d) Vertical MSE advection term ($\{\bar{\omega}\partial_p\bar{h}\}\$), net radiation term (\bar{F}_{net}), horizontal MSE advection term($-\{\bar{v}\cdot\nabla_p\bar{h}\}\$), and transient eddy term ($-\{\nabla_p\cdot\overline{(v'h')}\}\$) during low NHSI periods. (e)-(h) are the same as (a)-(d), but for the difference between high NHSI and low NHSI periods. The black rectangle is the NAF monsoon region.

Moving from low NHSI to high NHSI periods, the Sahara-Sahel region experiences increased energy input into the atmospheric column (Fig. 4f). This enhanced net energy forcing primarily stems from three factors (not shown in figures; Wen et al., 2022): First, greater shortwave radiation absorption due to increased cloud cover, which traps more solar radiation; second, increased surface latent heat flux resulting from higher rainfall and enhanced evaporation; and third, increased downwelling longwave radiation associated with deep convection. This convective activity promotes the formation of high-level clouds, which reduce outgoing longwave radiation and further amplify net energy into the atmospheric column. The increased net energy in the Sahara-Sahel region directly intensifies upward motion (Fig. 4e), leading to increased monsoon rainfall (Fig. 3c) and surface cooling in the region (Fig. 3b). Concurrently, strengthened southwesterly winds contribute to positive horizontal moist enthalpy advection (Fig. 4g), indicating energy transport from adjacent tropical high-MSE regions into the Sahara-Sahel. This horizontal energy flux further sustains the increased rainfall and expands the geographical influence of the monsoon system.

Additionally, we employ moisture tagging experiments to quantify the contributions of different moisture sources to the NAF monsoon rainfall response (Fig. 5). While the mean state rainfall in the NAF region is primarily supplied by the African continent (Fig. 5a1-a6), the rainfall increase from low NHSI periods to high NHSI periods is additionally contributed from the Atlantic Ocean (Fig. 5b1-b6). Quantitatively, the North Atlantic and South Atlantic Oceans together with the African continent account for over 80% of the total rainfall increase, with approximate contributions of 18% from the North Atlantic, 38% from the South Atlantic, and 28% from the African continent. These moisture contributions align with the dynamical framework in which intensified southwesterly monsoon winds enhance moisture transport from the Atlantic Ocean.





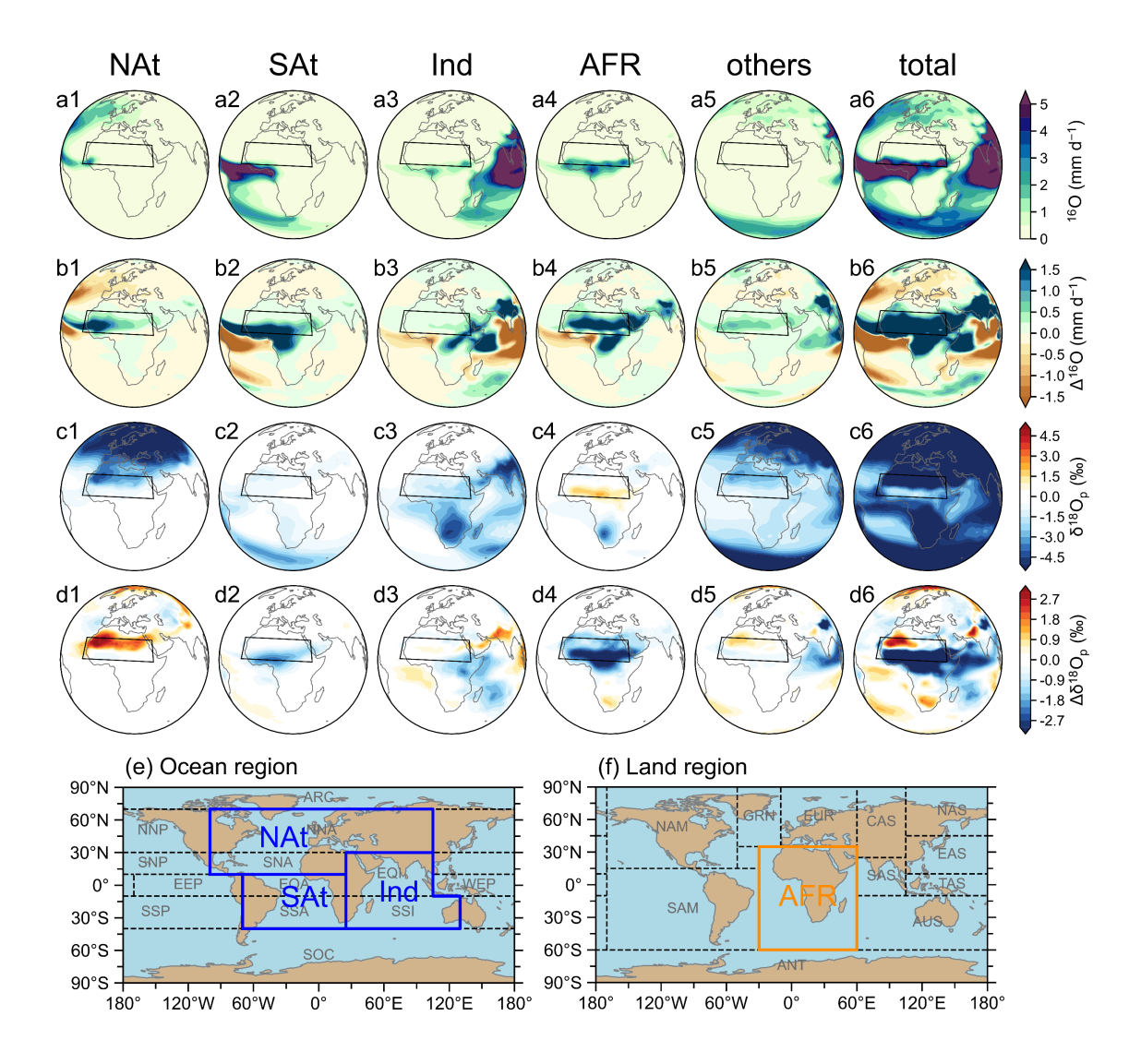


Figure 5: Tracking ^{16}O and $\delta^{18}O_p$ and their responses from source regions (high-low NHSI in tagging experiments). Summer climatological ^{16}O (mm d⁻¹) in low NHSI periods originating from moisture source regions (a1) North Atlantic Ocean (NAt), (a2) South Atlantic Ocean (SAt), (a3) Indian Ocean (Ind), (a4) African continent (AFR), (a5) other regions and (a6) the global total of 25 sub regions. (b1)-(b6) Same as (a1)-(a6) but for the ^{16}O difference between high and low NHSI periods. (c1)-(c6) Same as (a1)-(a6) but for climatology distribution of $\delta^{18}O_p$ (‰) during low NHSI periods. (d1)-(d6) Same as (b1)-(b6), but for the difference of $\delta^{18}O_p$ between high and low NHSI periods. The black rectangles mark the NAF monsoon region. (e) Regional divisions of the globe are used for tagging experiments. The black dashed boxes mark the ocean subregions used for the experiments. The blue polygons mark the regrouped ocean regions used for the analysis. (f) Similar to (e) but for land regions.

5 Mechanism of δ¹⁸O_p change

305

310

As illustrated above, $\delta^{18}O_p$ exhibits a dipole response with enrichment in the north but depletion in the south in response to high NHSI (Fig. 3e). Given the overall increase in rainfall across the NAF region, the change in $\delta^{18}O_p$ indicates a positive rainfall- $\delta^{18}O_p$ relationship in the north and negative relationship in the south. This contrast highlights the complexity of





regional $\delta^{18}O_p$ responses to external forcing and raises a critical question: Which hydrological processes are truly reflected by these $\delta^{18}O_p$ variations? To address this, we next employ moisture tagging experiments in iCAM5.3 to investigate the underlying mechanisms driving the $\delta^{18}O_p$ response.

Moisture tagging experiments perfectly reproduce meridional dipole pattern in $\delta^{18}O_p$ between high and low NHSI periods (Fig. 5d6). In light of this dipole response, we divide the monsoon region into two subregions for further analysis: a northern region (15°W-35°E, 18°N-25°N) and a southern region (15°W-35°E, 8°N-16°N). The tagging experiments indicate that the $\delta^{18}O_p$ variations in the NAF region are primarily influenced by moisture originating from the Atlantic Ocean and the African continent (Fig. 5d1 and d4), which is largely consistent with the rainfall changes discussed earlier. Specifically, the $\delta^{18}O_p$ enrichment in the northern region is mainly attributed to moisture from the North Atlantic, whereas depletion in the southern region is predominantly contributed by the South Atlantic and the African continent.

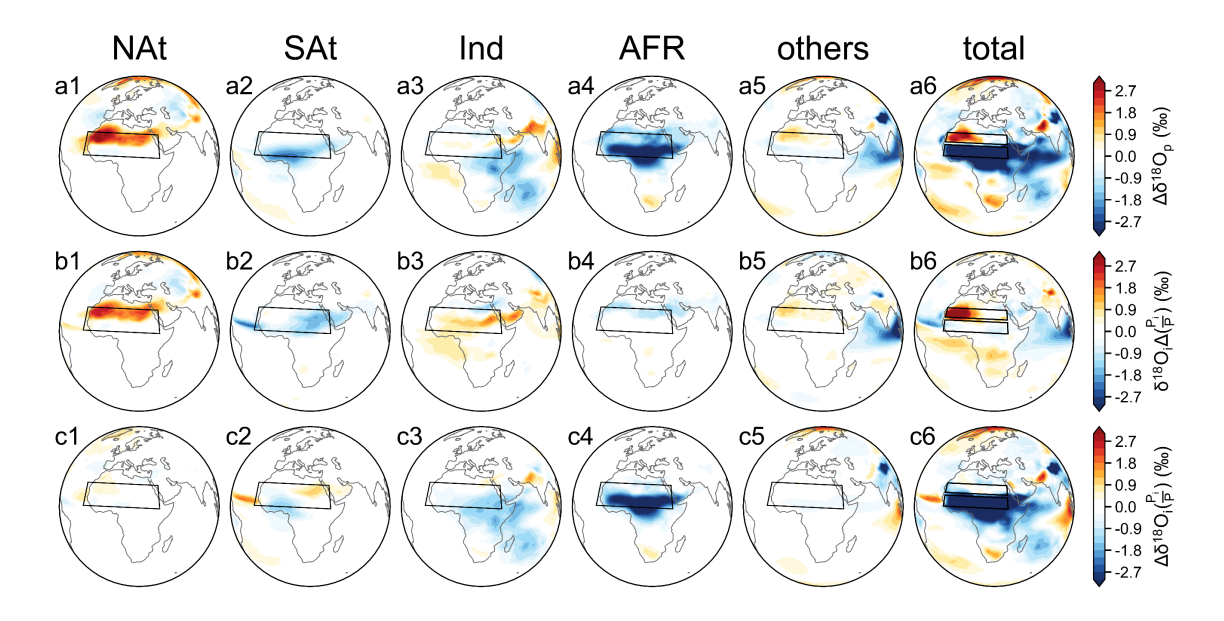


Figure 6: Decomposition $\delta^{18}O_p$ response from source regions (high-low NHSI in tagging experiments). (a1)-(a6) The $\delta^{18}O_p$ change from each source region, which is further decomposed into the changes due to (b1)-(b6) precipitation weight $\delta^{18}O_{pi} \cdot \Delta \left(\frac{P_i}{p}\right)$ and (c1)-(c6) $\delta^{18}O_p$ value $\frac{P_i}{p} \cdot \Delta \delta^{18}O_{pi}$. The $\delta^{18}O_p$ dipole regions are marked with black rectangles in (a6)-(c6).

To understand the mechanism behind the dipole response of $\delta^{18}O_p$, we first separate the changes in $\delta^{18}O_p$ (Fig. 6a) into two parts: the change associated with the precipitation weight $\Delta\left(\frac{P_i}{P}\right)$ (Fig. 6b) and change in the value of isotope ratio $\Delta\delta^{18}O_{pi}$ (Fig. 6c) based on the Eq. (5). The decomposition suggests that the northern and southern $\delta^{18}O_p$ response are influenced by different hydrological processes. The change related to precipitation weight provide almost all the positive $\delta^{18}O_p$ value in the northern NAF region (Fig. 6b), whereas the change in the value of isotope ratio is responsible for the negative $\delta^{18}O_p$ value in the south (Fig. 6c).

14





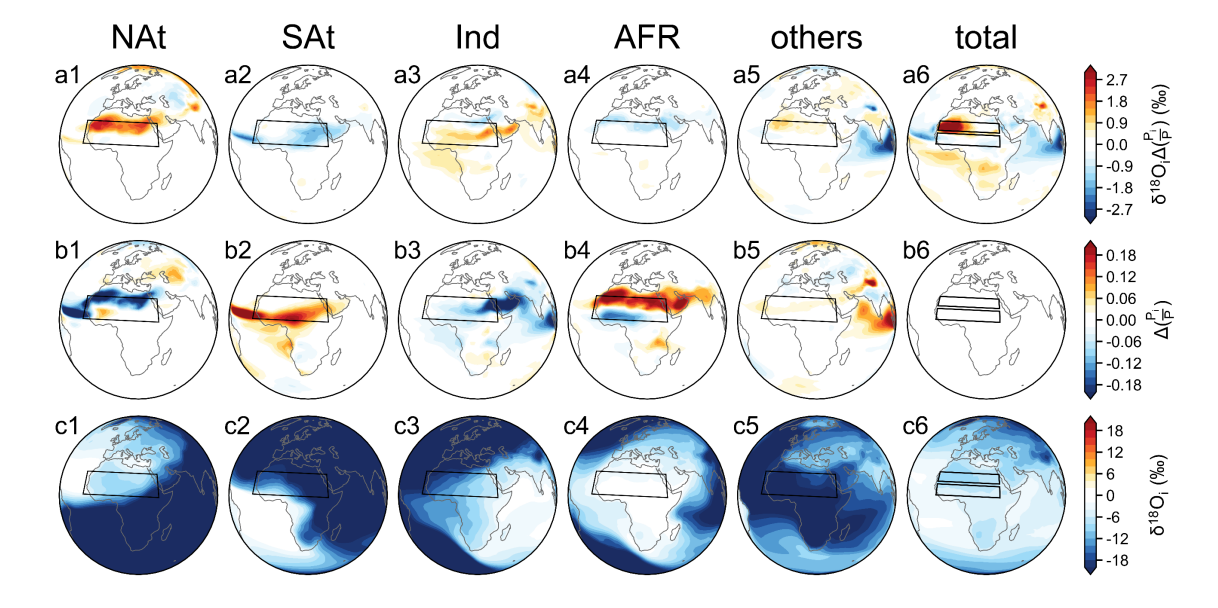


Figure 7: Decomposed $\delta^{18}O_p$ response induced by precipitation weight. (a1)-(a6) $\delta^{18}O_p$ response due to changes in precipitation weight $\delta^{18}O_{pi} \cdot \Delta\left(\frac{P_i}{p}\right)$. (b1)-(b6) Changes in precipitation weight $\Delta\left(\frac{P_i}{p}\right)$ from each source region. (c1)-(c6) Climatological $\delta^{18}O$ value from each source region.

Then, we focus on how changes in precipitation weight induces the $\delta^{18}O_p$ enrichment in the northern NAF region. The mean state rainfall in the region is mainly contributed by the moisture source from remote North Atlantic (32%) and local Africa (40%). From low to high NHSI periods, the precipitation weight from North Atlantic is decreased (Fig. 7b1), which is because the proportion of rainfall increase from North Atlantic is smaller than that from the total sources. In contrast, the precipitation contribution from African source increases (Fig. 7b4), due to enhanced monsoon rainfall (Fig. 3c). Consequently, the reduction of precipitation weight from North Atlantic (~-10%) is compensated by the increase of precipitation weight from African source (~11%). However, the $\delta^{18}O$ values from North Atlantic (~-7.8 %) are significantly more depleted compared to those from African source (~-2 %) (Fig. 7c1 vs c4). Thus, multiplying the $\delta^{18}O$ values by the changes in precipitation weight results in a net enrichment of $\delta^{18}O_p$. Therefore, during high NHSI periods, the relative reduction of distant moisture with more depleted $\delta^{18}O$ values, coupled with an increase in nearby moisture with more enriched $\delta^{18}O_p$ values, leads to a positive $\delta^{18}O_p$ response in the northern NAF region.

340

345



355

360

365



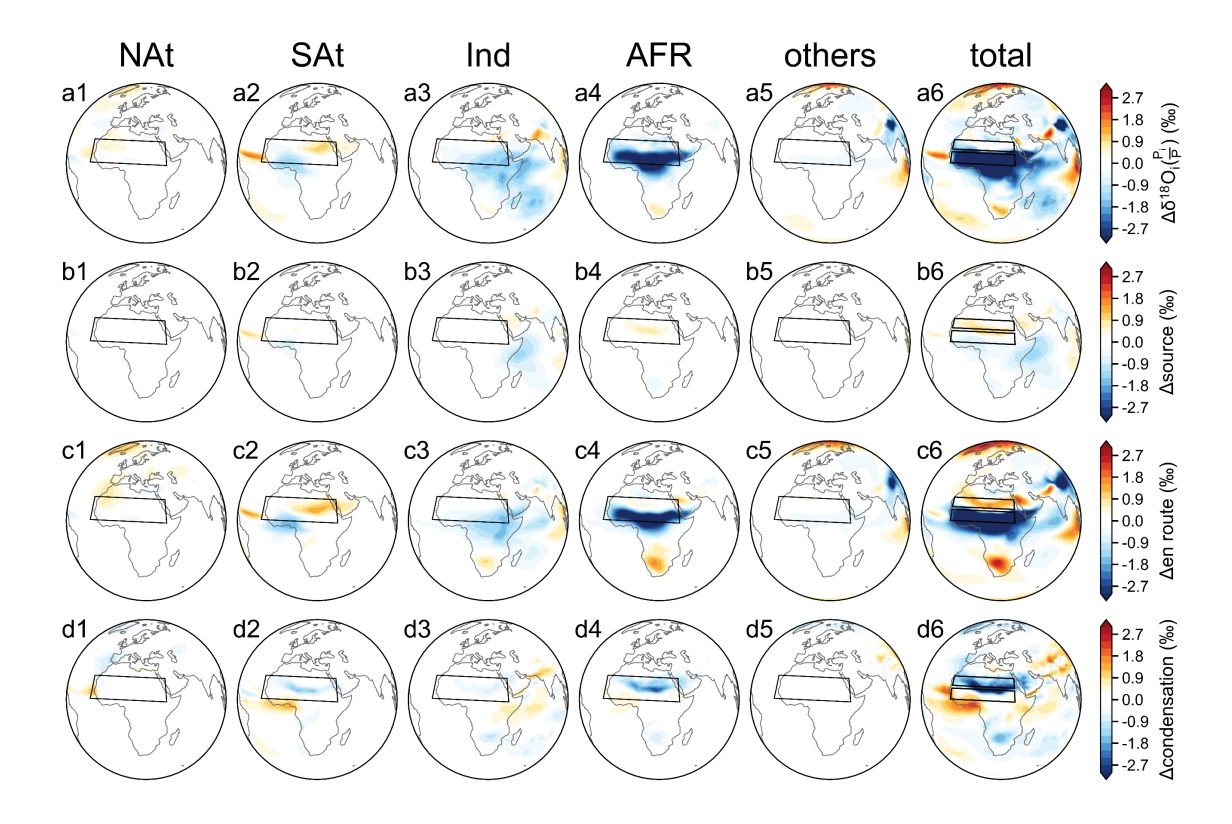


Figure 8: Decomposed $\delta^{18}O_p$ response induced by $\delta^{18}O_p$ value. (a1)-(a6) $\delta^{18}O_p$ response due to changes in $\delta^{18}O_p$ value $\frac{P_i}{P} \cdot \Delta \delta^{18}O_{pi}$, which are further decomposed into the change due to (b1)-(b6) source $\delta^{18}O_v$, (c1)-(c6) en route depletion and (d1)-(d6) condensation enrichment.

Finally, we examine how change in the value of isotope ratio leads to the negative $\delta^{18}O_p$ value in the southern NAF region. Our decomposition analysis (based on Eq. 6) shows that rainfall depletion from African continent (Fig. 8c4) determines the $\delta^{18}O_p$ depletion in the southern NAF region. This occurs because increased rainfall over the southern tropical region (Fig. 5b4) enhances rainout, resulting in more depleted vapor $\delta^{18}O$. This depleted moisture is then transported northward to the NAF monsoon region via southwest monsoon winds, undergoing further rainout along the trajectory and ultimately leading to more negative $\delta^{18}O$ values in the southern NAF region. Similarly, the en route depletion from South Atlantic and Indian Ocean sources is also partly responsible for $\delta^{18}O_p$ decrease in west and east of southern NAF region (Fig. 8c2 and c3), respectively, due to increased rainfall along their moisture pathway (Fig. 5b2 and b3). In contrast, the other two terms associated with source effect (Fig. 8b) and local condensation (Fig. 8d) have minimal influence on $\delta^{18}O_p$ changes in the region. This indicates that although rainfall and $\delta^{18}O_p$ are inversely related here, the depletion of $\delta^{18}O_p$ reflects the effect of upstream rainout rather than local rainfall amount.

However, in the arid-semi-arid Sahara-Sahel, the role of the local condensation change is not negligible. In the northern NAF region, the contribution of local rainfall condensation (Fig. 8d6) is relatively significant, but it is opposite to the total $\delta^{18}O_p$





enrichment response (Fig. 6a6). This suggests that the "amount effect" has only a limited role in these regions and its contribution is overwhelmed by other processes. Therefore, although this inverse relationship between NAF rainfall and $\delta^{18}O_p$ seems to be consistent with isotopic "amount effect", our study indicates that changes in NAF $\delta^{18}O_p$ cannot simply be attributed to local rainfall, but rather are influenced by a combination of multiple hydrological processes, which has important implications for the interpretation of variations in the speleothem $\delta^{18}O$ record.

6 Conclusions

370

380

385

390

In this study, to explore the climate interpretation of $\delta^{18}O_p$ in NAF monsoon region, we simulate climate and oxygen isotope evolutions to orbital forcing over the past 150,000 years using the iCESM. We find that the NAF hydroclimate is controlled by low-latitude insolation with a strong precessional signal. Spatially, the NAF monsoon region exhibits a regionally uniform increase in rainfall and a north-south dipole pattern in $\delta^{18}O_p$. In response to the enhanced NHSI, the increased solar radiation intensifies the land-sea thermal contrast, amplifying the pressure gradient and the southwest monsoon. The increased surface MSE and net energy input destabilizes the atmospheric structure and enhances vertical motion, thereby increasing monsoon rainfall in the NAF region. In terms of isotopic response, the change in dipole distribution in NAF suggests that $\delta^{18}O_p$ in this region is controlled by different hydrological processes. The results of tagging experiments suggest that δ¹⁸O_p enrichment in the northern NAF region is induced by changes in moisture sources, with a reduced contribution from distant regions and an increased role of local moisture. However, unlike the northern region, $\delta^{18}O_p$ depletion in the southern NAF region is mainly attributed to enhanced upstream rainfall along the moisture transport pathway. Our results indicate that the "amount effect" does not work in the southern NAF region, but alternately refers to upstream rainfall depletion from the African continent, enriching the current knowledge of isotope records in the region. But the decomposition of tagging experiments suggests that it is the upstream rainfall depletion from the African continent (this study) rather than the Atlantic Ocean (Shi et al., 2025) that dominates $\delta^{18}O_p$ changes in this region, which is different from previous knowledge. Our study reveals the complex mechanisms of oxygen isotope variations in the NAF monsoon region, providing new insights into the understanding of past climate and environmental changes in the region.

Similar to the NAF region, orbital-scale isotope simulations in other monsoon regions also show dipole patterns in $\delta^{18}O_p$. In Asia, Wen et al. (2024) identified a zonal grand dipole between South Asia (depleted $\delta^{18}O_p$) and Japan (enriched $\delta^{18}O_p$), driven by the changes in relative moisture from different source regions. In South America, there is similarly an opposite $\delta^{18}O_p$ variation in the Andes-Brazil (Liu and Battisti, 2015). Their analysis suggested that Andean $\delta^{18}O_p$ changes are associated with a change in the seasonality of precipitation and in the intensity of the upstream South American summer monsoon, while in northeastern Brazil the dominant role of rainfall intensity is very significant (Liu and Battisti, 2015). However, our study shows that local rainfall condensation has a very limited effect on NAF $\delta^{18}O_p$. This indicates that the "amount effect" has significant spatial heterogeneity and is not universally applicable in the tropics, as the role of other hydrological processes may be more important in these regions. Furthermore, distinct from the pronounced precession signal

https://doi.org/10.5194/egusphere-2025-5029 Preprint. Discussion started: 26 November 2025

© Author(s) 2025. CC BY 4.0 License.



405

EGUsphere Preprint repository

at low latitudes, the δ¹⁸O_p changes in North America primarily exhibit a 100-ka glacial-interglacial cycle and are eventually dominated by the ice volume forcing (Li et al., 2024). These results suggest that the dominant periodicities and forcing mechanisms of the orbital-scale δ¹⁸O_p variations in different regions are complex and varied.

Code and data availability

The ERA5 reanalysis publicly Climate data available from the Copernicus Change Service are (https://cds.climate.copernicus.eu/). The **GNIP** obtained **IAEA** data can be from the website (https://nucleus.iaea.org/wiser/explore/). Paleoclimate could be found **NOAA** proxy data from (https://www.ncei.noaa.gov/products/paleoclimatology). The iCESM modeling data and mapping code related to this article is available online at https://doi.org/10.5281/zenodo.17659273.

Author contribution

QW designed the experiments and carried them out. CJ performed the analysis, made the figures, and wrote the manuscript draft. QW worked on revising the manuscript. All authors were involved in helpful discussion and contributed to the manuscript.

Competing interests

The authors declare that they have no conflict of interest.

Acknowledgments

415 We thank Zhengyu Liu, Jian Liu, Deliang Chen, Liang Ning and Mi Yan for helpful discussions and Qiuzhen Yin for providing constructive reviews that improved the manuscript.

Financial support

This work is supported by the National Natural Science Foundation (NSF) of China (Nos. 42575051, 42130604, 42575050), National Key Research and Development Program of China (Grant No. 2023YFF0804700), Science and Technology Innovation Project of Laoshan Laboratory (LSKJ202203303), the State Key Laboratory of Loess and Quaternary Geology (SKLLQG2202).

References

Armitage, S. J., Bristow, C. S., and Drake, N. A.: West African monsoon dynamics inferred from abrupt fluctuations of Lake Mega-Chad, Proc. Natl. Acad. Sci., 112, 8543–8548, https://doi.org/10.1073/pnas.1417655112, 2015.





- Ayalon, A., Bar-Matthews, M., and Kaufman, A.: Climatic conditions during marine oxygen isotope stage 6 in the eastern Mediterranean region from the isotopic composition of speleothems of Soreq Cave, Israel, Geology, 30, 303–306, https://doi.org/10.1130/0091-7613(2002)030<0303:CCDMOI>2.0.CO;2, 2002.
 - Bao, Y., Liu, Z., and He, C.: Dipole Response of Millennial Variability in Tropical South American Precipitation and $\delta^{18}O_p$ during the Last Deglaciation. Part II: $\delta^{18}O_p$ Response, J. Clim., 36, 4709–4721, https://doi.org/10.1175/JCLI-D-22-0289.1, 2023.
 - Bar-Matthews, M., Ayalon, A., Gilmour, M., Matthews, A., and Hawkesworth, C. J.: Sea-land oxygen isotopic relationships from planktonic foraminifera and speleothems in the Eastern Mediterranean region and their implication for paleorainfall during interglacial intervals, Geochim. Cosmochim. Acta, 67, 3181–3199, https://doi.org/10.1016/S0016-7037(02)01031-1, 2003.
- Battisti, D. S., Ding, Q., and Roe, G. H.: Coherent pan-Asian climatic and isotopic response to orbital forcing of tropical insolation, J. Geophys. Res.: Atmos., 119, 11,997-12,020, https://doi.org/10.1002/2014JD021960, 2014.
 - Berger, A.: Long-term variations of caloric insolation resulting from the earth's orbital elements, Quat. Res., 9, 139–167, https://doi.org/10.1016/0033-5894(78)90064-9, 1978.
- Berger, A. and Pestiaux, P.: Accuracy and stability of the Quaternary terrestrial insolation, Milankovitch and Climate, 83–440 112, 1984.
 - Berger, A., Loutre, M., and Tricot, C.: Insolation and Earth's orbital periods, J. Geophys. Res., 98, 10341–10362, https://doi.org/10.1029/93JD00222, 1993.
 - Blanchet, C. L., Osborne, A. H., Tjallingii, R., Ehrmann, W., Friedrich, T., Timmermann, A., Brückmann, W., and Frank, M.: Drivers of river reactivation in North Africa during the last glacial cycle, Nat. Geosci., 14, 97–103, https://doi.org/10.1038/s41561-020-00671-3, 2021.
- Bosmans, J. H. C., Drijfhout, S. S., Tuenter, E., Hilgen, F. J., and Lourens, L. J.: Response of the North African summer monsoon to precession and obliquity forcings in the EC-Earth GCM, Clim. Dyn., 44, 279–297, https://doi.org/10.1007/s00382-014-2260-z, 2015.
 - Brady, E., Stevenson, S., Bailey, D., Liu, Z., Noone, D., Nusbaumer, J., Otto-Bliesner, B. L., Tabor, C., Tomas, R., Wong, T.,
- Zhang, J., and Zhu, J.: The Connected Isotopic Water Cycle in the Community Earth System Model Version 1, J. Adv. Model. Earth Syst., 11, 2547–2566, https://doi.org/10.1029/2019MS001663, 2019.
 - Brahim, Y. A., Sha, L., Wassenburg, J. A., Azennoud, K., Cheng, H., Cruz, F. W., and Bouchaou, L.: The spatiotemporal extent of the Green Sahara during the last glacial period, iScience, 26, 107018, https://doi.org/10.1016/j.isci.2023.107018, 2023.
- Cauquoin, A., Werner, M., and Lohmann, G.: Water isotopes climate relationships for the mid-Holocene and preindustrial period simulated with an isotope-enabled version of MPI-ESM, Clim. Past, 15, 1913–1937, https://doi.org/10.5194/cp-15-1913-2019, 2019.





- Chen, J. and Bordoni, S.: Orographic Effects of the Tibetan Plateau on the East Asian Summer Monsoon: An Energetic Perspective, J. Clim., 27, 3052–3072, https://doi.org/10.1175/JCLI-D-13-00479.1, 2014.
- Cheng, H., Sinha, A., Wang, X., Cruz, F. W., and Edwards, R. L.: The Global Paleomonsoon as seen through speleothem records from Asia and the Americas, Clim. Dyn., 39, 1045–1062, https://doi.org/10.1007/s00382-012-1363-7, 2012.
 Cheng, H., Sinha, A., Cruz, F. W., Wang, X., Edwards, R. L., d'Horta, F. M., Ribas, C. C., Vuille, M., Stott, L. D., and Auler,

A. S.: Climate change patterns in Amazonia and biodiversity, Nat. Commun., 4, 1411–1416, https://doi.org/10.1038/ncomms2415, 2013.

- Cheng, H., Edwards, R. L., Sinha, A., Spötl, C., Yi, L., Chen, S., Kelly, M., Kathayat, G., Wang, X., Li, X., Kong, X., Wang, Y., Ning, Y., and Zhang, H.: The Asian monsoon over the past 640,000 years and ice age terminations, Nature, 534, 640–646, https://doi.org/10.1038/nature18591, 2016.
 - Cheng H., Li H., Zhang X., Zhang H., Yi L., Cai Y., Hu Y., Shi Z., Peng Y., Zhao J., Gayatri K., and Ashish S.: European-Asian-African continent: An early form of supercontinent and supermonsoon, Quat. Sci., 40, 1381–1396,
- $470 \quad https://doi.org/10.11928/j.issn.1001-7410.2020.06.01, \ 2020.$
 - Cole, J. E., Rind, D., Webb, R. S., Jouzel, J., and Healy, R.: Climatic controls on interannual variability of precipitation δ^{18} O: Simulated influence of temperature, precipitation amount, and vapor source region, J. Geophys. Res.: Atmos., 104, 14223–14235, https://doi.org/10.1029/1999JD900182, 1999.
- Cook, K. H. and Vizy, E. K.: Contemporary Climate Change of the African Monsoon Systems, Curr. Clim. Change Rep., 5, 145–159, https://doi.org/10.1007/s40641-019-00130-1, 2019.
 - Coplen, T. B., Kendall, C., and Hopple, J.: Comparison of stable isotope reference samples, Nature, 302, 236–238, https://doi.org/10.1038/302236a0, 1983.
 - Crocker, A. J., Naafs, B. D. A., Westerhold, T., James, R. H., Cooper, M. J., Röhl, U., Pancost, R. D., Xuan, C., Osborne, C. P., Beerling, D. J., and Wilson, P. A.: Astronomically controlled aridity in the Sahara since at least 11 million years ago, Nat. Geosci., 15, 671–676, https://doi.org/10.1038/s41561-022-00990-7, 2022.
- Cruz, F. W., Burns, S. J., Karmann, I., Sharp, W. D., Vuille, M., Cardoso, A. O., Ferrari, J. A., Silva Dias, P. L., and Viana, O.: Insolation-driven changes in atmospheric circulation over the past 116,000 years in subtropical Brazil, Nature, 434, 63–66, https://doi.org/10.1038/nature03365, 2005.
 - Dansgaard, W.: Stable isotopes in precipitation, Tellus, 16, 436–468, https://doi.org/10.3402/tellusa.v16i4.8993, 1964.
- Datti, A. D., Zeng, G., Monerie, P.-A., Oo, K. T., and Chen, C.: A Review of the arctic-West African monsoon nexus: How arctic sea ice decline influences monsoon system, Theor. Appl. Climatol., 156, 9–29, https://doi.org/10.1007/s00704-024-05255-4, 2025.
 - deMenocal, P., Ortiz, J., Guilderson, T., and Sarnthein, M.: Coherent High- and Low-Latitude Climate Variability During the Holocene Warm Period, Science, 288, 2198–2202, https://doi.org/10.1126/science.288.5474.2198, 2000.
- deMenocal, P. B.: African climate change and faunal evolution during the Pliocene–Pleistocene, Earth Planet. Sci. Lett., 220, 3–24, https://doi.org/10.1016/S0012-821X(04)00003-2, 2004.





- deMenocal, P. B. and Tierney, J. E.: Green Sahara: African Humid Periods paces by Earth's orbital changes, Nat Educ Knowl., 3, 12–17, 2012.
- Ehrmann, W., Schmiedl, G., Seidel, M., Krüger, S., and Schulz, H.: A distal 140 kyr sediment record of Nile discharge and East African monsoon variability, Clim. Past, 12, 713–727, https://doi.org/10.5194/cp-12-713-2016, 2016.
 - Ehrmann, W., Schmiedl, G., Beuscher, S., and Krüger, S.: Intensity of African Humid Periods Estimated from Saharan Dust Fluxes, PloS ONE, 12, e0170989, https://doi.org/10.1371/journal.pone.0170989, 2017.
 - Fersi, W., Lézine, A.-M., and Bassinot, F.: Hydro-climate changes over southwestern Arabia and the Horn of Africa during the last glacial–interglacial transition: A pollen record from the Gulf of Aden, Rev. Palaeobot. Palynol., 233, 176–185, https://doi.org/10.1016/j.revpalbo.2016.04.002, 2016.
 - Grant, K. M., Grimm, R., Mikolajewicz, U., Marino, G., Ziegler, M., and Rohling, E. J.: The timing of Mediterranean sapropel deposition relative to insolation, sea-level and African monsoon changes, Quat. Sci. Rev., 140, 125–141, https://doi.org/10.1016/j.quascirev.2016.03.026, 2016.
- Grant, K. M., Rohling, E. J., Westerhold, T., Zabel, M., Heslop, D., Konijnendijk, T., and Lourens, L.: A 3 million year index for North African humidity/aridity and the implication of potential pan-African Humid periods, Quat. Sci. Rev., 171, 100–118, https://doi.org/10.1016/j.quascirev.2017.07.005, 2017.
 - He, C., Liu, Z., Otto-Bliesner, B. L., Brady, E. C., Zhu, C., Tomas, R., Clark, P. U., Zhu, J., Jahn, A., Gu, S., Zhang, J., Nusbaumer, J., Noone, D., Cheng, H., Wang, Y., Yan, M., and Bao, Y.: Hydroclimate footprint of pan-Asian monsoon water isotope during the last deglaciation, Sci. Adv., 7, eabe2611, https://doi.org/10.1126/sciadv.abe2611, 2021.
- Herold, M. and Lohmann, G.: Eemian tropical and subtropical African moisture transport: an isotope modelling study, Clim. Dyn., 33, 1075–1088, https://doi.org/10.1007/s00382-008-0515-2, 2009.
 - Hill, S. A., Ming, Y., Held, I. M., and Zhao, M.: A Moist Static Energy Budget–Based Analysis of the Sahel Rainfall Response to Uniform Oceanic Warming, J. Clim., 30, 5637–5660, https://doi.org/10.1175/JCLI-D-16-0785.1, 2017.
- Hu, J., Emile-Geay, J., Tabor, C., Nusbaumer, J., and Partin, J.: Deciphering Oxygen Isotope Records From Chinese Speleothems With an Isotope-Enabled Climate Model, Paleoceanogr. Paleoclimatol., 34, 2098–2112, https://doi.org/10.1029/2019PA003741, 2019.
 - Hunke, E. C.: Thickness sensitivities in the CICE sea ice model, Ocean Model., 34, 137–149, https://doi.org/10.1016/j.ocemod.2010.05.004, 2010.
- Kohfeld, K. E. and Harrison, S. P.: How well can we simulate past climates? Evaluating the models using global palaeoenvironmental datasets, Quat. Sci. Rev., 19, 321–346, https://doi.org/10.1016/S0277-3791(99)00068-2, 2000.
 - Kurita, N.: Water isotopic variability in response to mesoscale convective system over the tropical ocean, J. Geophys. Res.: Atmos., 118, 10,376-10,390, https://doi.org/10.1002/jgrd.50754, 2013.
 - Kutzbach, J. E. and Liu, Z.: Response of the African Monsoon to Orbital Forcing and Ocean Feedbacks in the Middle Holocene, Science, 278, 440–443, https://doi.org/10.1126/science.278.5337.440, 1997.



530

540



- Kutzbach, J. E., Liu, X., Liu, Z., and Chen, G.: Simulation of the evolutionary response of global summer monsoons to orbital forcing over the past 280,000 years, Clim. Dyn., 30, 567–579, https://doi.org/10.1007/s00382-007-0308-z, 2008.
 Kutzbach, J. E., Guan, J., He, F., Cohen, A. S., Orland, I. J., and Chen, G.: African climate response to orbital and glacial forcing in 140,000-y simulation with implications for early modern human environments, PNAS, 117, 2255–2264, https://doi.org/10.1073/pnas.1917673117, 2020.
- Process., 22, 1–8, https://doi.org/10.1002/hyp.6637, 2007.

 Lee, J.-E., Johnson, K., and Fung, I.: Precipitation over South America during the Last Glacial Maximum: An analysis of the "amount effect" with a water isotope-enabled general circulation model, Geophys. Res. Lett., 36, https://doi.org/10.1029/2009GL039265, 2009.

Lee, J.-E. and Fung, I.: "Amount effect" of water isotopes and quantitative analysis of post-condensation processes, Hydrol.

- Lézine, A.-M., Duplessy, J.-C., and Cazet, J.-P.: West African monsoon variability during the last deglaciation and the Holocene: Evidence from fresh water algae, pollen and isotope data from core KW31, Gulf of Guinea, PALAEOGEOGR PALAEOCL, 219, 225–237, https://doi.org/10.1016/j.palaeo.2004.12.027, 2005.
 - Lézine, A.-M., Hély, C., Grenier, C., Braconnot, P., and Krinner, G.: Sahara and Sahel vulnerability to climate changes, lessons from Holocene hydrological data, Quat. Sci. Rev., 30, 3001–3012, https://doi.org/10.1016/j.quascirev.2011.07.006, 2011.
 - Li, Y., Liu, X., Xie, X., and Yin, Z.: Diverse Orbital-Scale Variations of Precipitation Oxygen Isotopes in the Northern Hemisphere Mid-Latitudes: A Comparative Study Between East Asia and North America, Paleoceanogr. Paleoclimatol., 39, e2024PA004914, https://doi.org/10.1029/2024PA004914, 2024.
- Liu, X. and Battisti, D. S.: The Influence of Orbital Forcing of Tropical Insolation on the Climate and Isotopic Composition of Precipitation in South America, J. Clim., 28, 4841–4862, https://doi.org/10.1175/JCLI-D-14-00639.1, 2015.
- Liu, Z., Wen, X., Brady, E. C., Otto-Bliesner, B., Yu, G., Lu, H., Cheng, H., Wang, Y., Zheng, W., Ding, Y., Edwards, R. L., Cheng, J., Liu, W., and Yang, H.: Chinese cave records and the East Asia Summer Monsoon, Quat. Sci. Rev., 83, 115–128, https://doi.org/10.1016/j.quascirev.2013.10.021, 2014.
- Lorenz, S. J. and Lohmann, G.: Acceleration technique for Milankovitch type forcing in a coupled atmosphere-ocean circulation model: method and application for the Holocene, Clim. Dyn., 23, 727–743, https://doi.org/10.1007/s00382-004-0469-y, 2004.
 - Marzocchi, A., Lunt, D. J., Flecker, R., Bradshaw, C. D., Farnsworth, A., and Hilgen, F. J.: Orbital control on late Miocene climate and the North African monsoon: insight from an ensemble of sub-precessional simulations, Clim. Past, 11, 1271–1295, https://doi.org/10.5194/cp-11-1271-2015, 2015.
- McDougall, I., Brown, F. H., and Fleagle, J. G.: Stratigraphic placement and age of modern humans from Kibish, Ethiopia, Nature, 433, 733–736, https://doi.org/10.1038/nature03258, 2005.





- Messori, G., Gaetani, M., Zhang, Q., Zhang, Q., and Pausata, F. S. R.: The water cycle of the mid-Holocene West African monsoon: The role of vegetation and dust emission changes, Int. J. Climatol., 39, 1927–1939, https://doi.org/10.1002/joc.5924, 2019.
- Moore, M., Kuang, Z., and Blossey, P. N.: A moisture budget perspective of the amount effect, Geophys. Res. Lett., 41, 1329–1335, https://doi.org/10.1002/2013GL058302, 2014.
 - Muschitiello, F., Zhang, Q., Sundqvist, H. S., Davies, F. J., and Renssen, H.: Arctic climate response to the termination of the African Humid Period, Quat. Sci. Rev., 125, 91–97, https://doi.org/10.1016/j.quascirev.2015.08.012, 2015.
 - Neale, R. B., Chen, C.-C., Gettelman, A., Lauritzen, P. H., Park, S., Williamson, D. L., Conley, A. J., Garcia, R., Kinnison,
- 565 D., Lamarque, J.-F., and others: Description of the NCAR community atmosphere model (CAM 5.0), NCAR Tech Note NCARTN-486 STR, 1, 1–12, 2010.
 - Nusbaumer, J., Wong, T. E., Bardeen, C., and Noone, D.: Evaluating hydrological processes in the Community Atmosphere Model Version 5 (CAM5) using stable isotope ratios of water, J. Adv. Model. Earth Syst., 9, 949–977, https://doi.org/10.1002/2016MS000839, 2017.
- Oleson, K. W., Lawrence, D. M., Flanner, M. G., Kluzek, E., Levis, S., Swenson, S. C., Thornton, E., Dai, A., Decker, M., Dickinson, R., Feddema, J., Heald, C. L., Lamarque, J.-F., Niu, G.-Y., Qian, T., Running, S., Sakaguchi, K., Slater, A., Stöckli, R., Wang, A., Yang, L., Zeng, X., and Zeng, X.: Technical Description of version 4.0 of the Community Land Model (CLM), NCAR Tech Note NCARTN-4781STR, 257, https://doi.org/10.5065/D6FB50WZ, 2010.
 - O'Mara, N. A., Skonieczny, C., McGee, D., Winckler, G., Bory, A. J.-M., Bradtmiller, L. I., Malaizé, B., and Polissar, P. J.:
- 575 Pleistocene drivers of Northwest African hydroclimate and vegetation, Nat. Commun., 13, 3552, https://doi.org/10.1038/s41467-022-31120-x, 2022.
 - O'Neil, J. R., Clayton, R. N., and Mayeda, T. K.: Oxygen Isotope Fractionation in Divalent Metal Carbonates, J. Chem. Phys., 51, 5547–5558, https://doi.org/10.1063/1.1671982, 1969.
- Patricola, C. M. and Cook, K. H.: Dynamics of the West African Monsoon under Mid-Holocene Precessional Forcing: Regional Climate Model Simulations, J. Clim., 20, 694–716, https://doi.org/10.1175/JCLI4013.1, 2007.
 - Pausata, F. S. R., Battisti, D. S., Nisancioglu, K. H., and Bitz, C. M.: Chinese stalagmite δ^{18} O controlled by changes in the Indian monsoon during a simulated Heinrich event, Nat. Geosci., 4, 474–480, https://doi.org/10.1038/ngeo1169, 2011.
 - Pausata, F. S. R., Messori, G., and Zhang, Q.: Impacts of dust reduction on the northward expansion of the African monsoon during the Green Sahara period, Earth Planet. Sci. Lett., 434, 298–307, https://doi.org/10.1016/j.epsl.2015.11.049, 2016.
- Pausata, F. S. R., Gaetani, M., Messori, G., Berg, A., Maia De Souza, D., Sage, R. F., and deMenocal, P. B.: The Greening of the Sahara: Past Changes and Future Implications, One Earth, 2, 235–250, https://doi.org/10.1016/j.oneear.2020.03.002, 2020.
 - Pokras, E. M. and Mix, A. C.: Earth's precession cycle and Quaternary climatic change in tropical Africa, Nature, 326, 486–487, https://doi.org/10.1038/326486a0, 1987.





- Revel, M., Ducassou, E., Grousset, F. E., Bernasconi, S. M., Migeon, S., Revillon, S., Mascle, J., Murat, A., Zaragosi, S., and Bosch, D.: 100,000 Years of African monsoon variability recorded in sediments of the Nile margin, Quat. Sci. Rev., 29, 1342–1362, https://doi.org/10.1016/j.quascirev.2010.02.006, 2010.
 - Risi, C., Bony, S., and Vimeux, F.: Influence of convective processes on the isotopic composition (δ¹⁸O and δD) of precipitation and water vapor in the tropics: 2. Physical interpretation of the amount effect, J. Geophys. Res.: Atmos., 113, 306, https://doi.org/10.1029/2008JD009943, 2008.
 - Roe, G. H., Ding, Q., Battisti, D. S., Molnar, P., Clark, M. K., and Garzione, C. N.: A modeling study of the response of Asian summertime climate to the largest geologic forcings of the past 50 Ma, J. Geophys. Res.: Atmos, 121, 5453–5470, https://doi.org/10.1002/2015JD024370, 2016.
- Rohling, E. J., Marino, G., and Grant, K. M.: Mediterranean climate and oceanography, and the periodic development of anoxic events (sapropels), Earth-Sci. Rev., 143, 62–97, https://doi.org/10.1016/j.earscirev.2015.01.008, 2015.
 - Rose, C., Polissar, P. J., Tierney, J. E., Filley, T., and deMenocal, P. B.: Changes in northeast African hydrology and vegetation associated with Pliocene–Pleistocene sapropel cycles, Philos. Trans. R. Soc. B, 371, 20150243, https://doi.org/10.1098/rstb.2015.0243, 2016.
- Rozanski, K., Araguás-Araguás, L., and Gonfiantini, R.: Isotopic Patterns in Modern Global Precipitation, Geophys. Monogr. Ser., 78, 1–36, https://doi.org/10.1029/GM078p0001, 1993.
 - Schneider, T., Bischoff, T., and Haug, G. H.: Migrations and dynamics of the intertropical convergence zone, Nature, 513, 45–53, https://doi.org/10.1038/nature13636, 2014.
 - Selami, N., Sèze, G., Gaetani, M., Grandpeix, J.-Y., Flamant, C., Cuesta, J., and Benabadji, N.: Cloud Cover over the Sahara during the Summer and Associated Circulation Features, Atmosphere, 12, 428–460, https://doi.org/10.3390/atmos12040428, 2021.
 - Shi, X., Cauquoin, A., Lohmann, G., Jonkers, L., Wang, Q., Yang, H., Sun, Y., and Werner, M.: Simulated stable water isotopes during the mid-Holocene and pre-industrial periods using AWI-ESM-2.1-wiso, Geosci. Model Dev., 16, 5153–5178, https://doi.org/10.5194/gmd-16-5153-2023, 2023.
 - Shi, X., Werner, M., Pausata, F. S. R., Yang, H., Liu, J., D'Agostino, R., Ingrosso, R., Yang, C., Gao, Q., and Lohmann, G.:
- On the length and intensity of the West African summer monsoon during the last interglacial African humid period, Quat. Sci. Rev., 328, 108542, https://doi.org/10.1016/j.quascirev.2024.108542, 2024.
 - Shi, X., Werner, M., Yang, H., Gao, Q., Liu, J., and Lohmann, G.: Precession Controls on Climate and Water Isotope Signals in Northern Africa, Paleoceanogr. Paleoclimatol., 40, e2024PA004999, https://doi.org/10.1029/2024PA004999, 2025.
- 620 Skonieczny, C., McGee, D., Winckler, G., Bory, A., Bradtmiller, L. I., Kinsley, C. W., Polissar, P. J., De Pol-Holz, R., Rossignol, L., and Malaizé, B.: Monsoon-driven Saharan dust variability over the past 240,000 years, Sci. Adv., 5, eaav1887, https://doi.org/10.1126/sciadv.aav1887, 2019.





- Smith, R., Jones, P., Briegleb, B., Bryan, F., Danabasoglu, G., Dennis, J., Dukowicz, J., Eden, C., Fox-Kemper, B., Gent, P., and others: The parallel ocean program (POP) reference manual: Ocean component of the community climate system model (CCSM), LAUR-01853, 141, 1–141, 2010.
- Sultan, B. and Gaetani, M.: Agriculture in West Africa in the Twenty-First Century: Climate Change and Impacts Scenarios, and Potential for Adaptation, Front. Plant Sci., 7, 1262, https://doi.org/10.3389/fpls.2016.01262, 2016.

 Sultan, B. Baron, C. Dingkuhn, M. Sarr, B. and Janicot, S.: Agricultural impacts of large scale variability of the West
- Sultan, B., Baron, C., Dingkuhn, M., Sarr, B., and Janicot, S.: Agricultural impacts of large-scale variability of the West African monsoon, Agric. For. Meteorol., 128, 93–110, https://doi.org/10.1016/j.agrformet.2004.08.005, 2005.
- Tabor, C. R., Otto-Bliesner, B. L., Brady, E. C., Nusbaumer, J., Zhu, J., Erb, M. P., Wong, T. E., Liu, Z., and Noone, D.: Interpreting Precession-Driven δ¹⁸O Variability in the South Asian Monsoon Region, J. Geophys. Res.: Atmos., 123, 5927–5946, https://doi.org/10.1029/2018JD028424, 2018.
 - Tierney, J. E., Pausata, F. S. R., and deMenocal, P. B.: Rainfall regimes of the Green Sahara, Sci. Adv., 3, e1601503, https://doi.org/10.1126/sciadv.1601503, 2017.
- Timm, O. and Timmermann, A.: Simulation of the Last 21 000 Years Using Accelerated Transient Boundary Conditions, J. Clim., 20, 4377–4401, https://doi.org/10.1175/JCLI4237.1, 2007.
 - Tuenter, E., Weber, S. L., Hilgen, F. J., and Lourens, L. J.: The response of the African summer monsoon to remote and local forcing due to precession and obliquity, Global Planet. Change, 36, 219–235, https://doi.org/10.1016/S0921-8181(02)00196-0, 2003.
- Vaks, A., Bar-Matthews, M., Ayalon, A., Matthews, A., Halicz, L., and Frumkin, A.: Desert speleothems reveal climatic window for African exodus of early modern humans, Geology, 35, 831–834, https://doi.org/10.1130/G23794A.1, 2007.
 Vuille, M., Bradley, R. S., Werner, M., Healy, R., and Keimig, F.: Modeling δ¹8O in precipitation over the tropical Americas:
 1. Interannual variability and climatic controls, J. Geophys. Res.: Atmos., 108, 4174, https://doi.org/10.1029/2001JD002038, 2003.
- Waldmann, N., Torfstein, A., and Stein, M.: Northward intrusions of low- and mid-latitude storms across the Saharo-Arabian belt during past interglacials, Geology, 38, 567–570, https://doi.org/10.1130/G30654.1, 2010.
 Wang, Y. J., Cheng, H., Edwards, R. L., An, Z. S., Wu, J. Y., Shen, C.-C., and Dorale, J. A.: A High-Resolution Absolute-
 - Dated Late Pleistocene Monsoon Record from Hulu Cave, China, Science, 294, 2345–2348, https://doi.org/10.1126/science.1064618, 2001.
- Weber, S. L. and Tuenter, E.: The impact of varying ice sheets and greenhouse gases on the intensity and timing of boreal summer monsoons, Quat. Sci. Rev., 30, 469–479, https://doi.org/10.1016/j.quascirev.2010.12.009, 2011.
 - Wen, Q., Liu, Z., Zhu, J., Yan, M., He, C., Han, J., Liu, J., and Liang, Y.: Local Insolation Drives Afro-Asian Monsoon at Orbital-Scale in Holocene, Geophys. Res. Lett., 49, e2021GL097661, https://doi.org/10.1029/2021GL097661, 2022.
- Wen, Q., Liu, Z., Jing, Z., Clemens, S. C., Wang, Y., Yan, M., Ning, L., and Liu, J.: Grand dipole response of Asian summer
- 655 monsoon to orbital forcing, Npj Clim. Atmospheric Sci., 7, 1–11, https://doi.org/10.1038/s41612-024-00749-4, 2024.





Yin, Q. and Berger, A.: Interglacial analogues of the Holocene and its natural near future, Quat. Sci. Rev., 120, 28–46, https://doi.org/10.1016/j.quascirev.2015.04.008, 2015.

Ziegler, M., Tuenter, E., and Lourens, L. J.: The precession phase of the boreal summer monsoon as viewed from the eastern Mediterranean (ODP Site 968), Quat. Sci. Rev., 29, 1481–1490, https://doi.org/10.1016/j.quascirev.2010.03.011, 2010.